



Investigation of fluidic thrust vectoring for scramjets

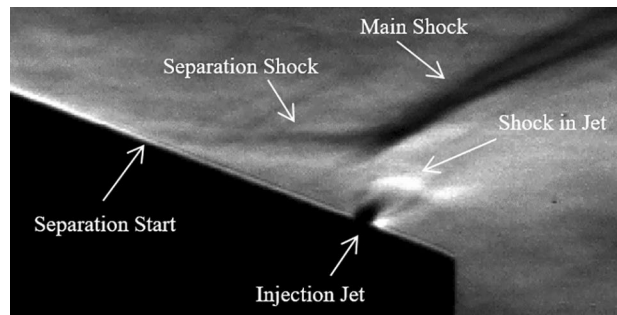
Chris Hambidge¹ · William Ivison¹ · David Steuer² · Andrew Neely³ · Matthew McGilvray¹

Received: 21 December 2021 / Revised: 20 January 2023 / Accepted: 12 February 2023 / Published online: 25 March 2023
© The Author(s) 2023

Abstract

Fluidic thrust vectoring (FTV) offers a novel approach to aerodynamic control, circumventing some of the issues associated with mechanical systems. One method is shock vector control which involves injecting a fluid into the exhaust nozzle of an engine to redirect the gases and thus, produce a control force. An experimental model which incorporated FTV was designed and tested at Mach 6 in the Oxford high density tunnel (HDT). The model was a simplified two-dimensional scramjet geometry with two different configurations to compare an internal and external exhaust nozzle. The FTV injection system consisted of a slot at the rear edge of the exhaust nozzle fed from an internal plenum. In the experimental campaign, a range of gas injection pressures and free stream stagnation pressures were tested to assess the effectiveness of both configurations. Two new measurement methods were successfully implemented in the HDT: pressure sensitive paint and a 6-axis load cell. The FTV system has been shown to be effective with observable increases in lift and pitching moment. A linear relation between the injection pressure ratio and the control forces could be observed for both configurations.

Graphical abstract



1 Introduction

Aerodynamic control of hypersonic vehicles is traditionally achieved using mechanical control surfaces (Skujins et al. 2010). However, components for such arrangements tend to

be very thin to minimize drag at hypersonic speeds and so they are more susceptible to the thermal effects of aerodynamic heating (Van Wie et al. 2004). An alternative method of control is thrust vectoring, where the exhaust from an engine is diverted away from the axis of motion, creating

✉ Chris Hambidge
chris.hambidge@eng.ox.ac.uk

William Ivison
william.ivison@eng.ox.ac.uk

David Steuer
dsteuer@irs.uni-stuttgart.de

Andrew Neely
a.neely@adfa.edu.au

Matthew McGilvray
matthew.mcgilvray@eng.ox.ac.uk

¹ Oxford Thermofluids Institute, University of Oxford, Oxford, UK

² Faculty of Aerospace Engineering and Geodesy, University of Stuttgart, Stuttgart, Germany

³ School of Engineering and Information Technology, University of New South Wales Canberra, Canberra, Australia

a pitching force on the aircraft. Mechanical thrust vector control systems currently used to achieve vectoring are very heavy and add significant complexity to an aircraft.

Fluidic thrust vectoring (FTV) can offer an alternative solution to mechanical systems, where a secondary fluid is injected into the exhaust nozzle of an engine causing a deflection of the exhaust stream away from the injection site. FTV systems are mechanically very simple and do not need the heavy components associated with mechanical thrust vectoring. Although no practical working examples have been demonstrated for hypersonic flight, such systems are aimed at allowing for reduced size and complexity of aerodynamic control surfaces on hypersonic vehicles.

The force achievable from secondary jet injection is larger than that of just the injector thrust on its own. This is commonly referred to as the amplification or magnification factor (Wu 1961; Spaid 1975). The underlying cause is the increase in surface pressure upstream of the injector due to shock-induced boundary layer separation. Looking at this from a control volume perspective, this results in the nozzle exit flow being diverted and distortion of the exit pressure profile. The amplification factor has been shown to be insensitive to most factors of the exhaust flow (Mach number, Reynolds number, jet diameter) (Spaid 1975). However, the amplification factor is increased with decreasing ratio of jet total pressure to local exhaust pressure (Spaid 1975). Thus, applying this in the nozzle exhaust will give higher forces due to the higher pressures in comparison with the external vehicle surface. The rear end of the exhaust also provides the longest lever arm on the engine, naturally providing larger moments. The optimal location is therefore dependent of nozzle/vehicle design and would need to be incorporated during the earlier stages of design.

This paper extends the work of Ivison et al. (2019) to include further testing and analysis of an internal nozzle configuration. The model was developed with a slot injector mounted to the exhaust. Two exhaust nozzle configurations, internal and external (referred to as *long* and *short* cowl, respectively), were tested under a variety of freestream conditions and injection pressure ratios.

2 Experimental setup

2.1 Oxford high density tunnel

Testing took place in the Oxford High Density Tunnel (HDT), operated as a heated Ludwieg Tunnel. The facility features a 152-mm-diameter, 17.3-m-long barrel that can be pre-heated up to 550 K. A Mach 6 contoured nozzle with an exit diameter of 350 mm was used. The initial fill conditions are set to meet the desired stagnation pressure and temperature in the test, which are directly measured. The

facility produces successive periods of steady flow, each lasting approximately 40–50 ms, set by the plug opening time, stagnation plenum volume, nozzle throat diameter and the transit of the unsteady expansion waves along the facility. Further details about the Oxford HDT can be found in McGilvray et al. (2015).

The freestream conditions produced for the testing are detailed in Table 1. These are calculated assuming isentropic expansion of air through the nozzle, using the measured stagnation pressure averaged over steady periods of 30–40 ms together with calibrated Mach number and total temperature relations. The viscosity is calculated via the Keyes relation (Keyes and Frederick 1952). To enable injection of a control flow, a new gas injection system was implemented in the HDT (Ivison et al. 2019). Timings were set so that the pressure in the model's plenum reached a steady level before the tunnel was fired. The drop in plenum pressure over each test was < 1%.

2.2 Experimental model

The experimental model was designed as a 2D generic scramjet shape, following a similar geometry to Van Pelt et al. (2017). The dual-ramp intake compresses the freestream flow before expanding it through a 19 degree straight-sided nozzle. The injector was located on the body side, 10 mm from the downstream end of the 100-mm-long exhaust ramp. Figure 1 presents CAD images of the model, which is 311.6 mm long and 80 mm wide. This configuration thus formed a 2D generic analogue of an external expansion scramjet nozzle like that used on the NASA X-43 McClinton (2006), mounted upside down. For further comparison, a second configuration of the model was designed with long side walls and a long top cowl to form an internal expansion scramjet nozzle (Fig. 1). The whole model was mounted to a 6-axis load cell and shielded to prevent aerodynamic loading of the support and load cell. The injector was slot-like and contained six closely spaced individual two-dimensional nozzles which were choked to ensure the mass flow rate was independent of the freestream. The nozzles had a total throat

Table 1 Nominal flow properties for experiments in the HDT

Condition	Mach number	Total pressure	Total temperature (MPa)	Re_{unit} ($10^6/m$) (K)
1	6.00 ± 0.03	1.85 ± 0.04	385 ± 15	21.3 ± 1.7
2	6.00 ± 0.04	1.60 ± 0.04	384 ± 15	18.5 ± 1.5
3	6.00 ± 0.05	1.39 ± 0.04	383 ± 15	16.1 ± 1.5
4	6.00 ± 0.06	1.13 ± 0.04	385 ± 15	13.0 ± 1.3
5	6.00 ± 0.06	0.98 ± 0.04	384 ± 15	11.3 ± 1.3
6	6.00 ± 0.07	0.85 ± 0.04	384 ± 15	9.8 ± 1.2

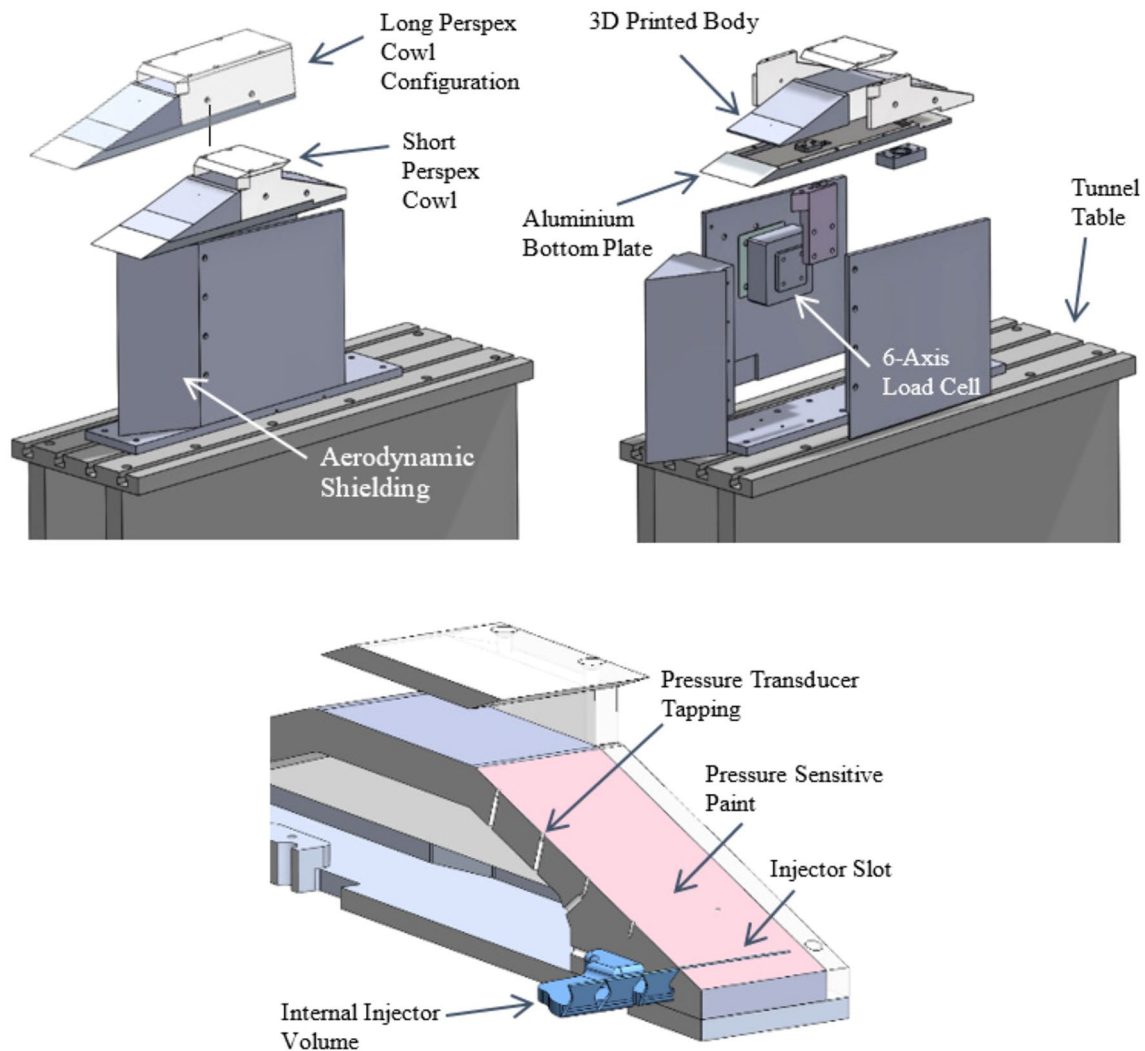


Fig. 1 CAD images of the FTV model with shielding and injector volume

area of 25.2 mm^2 and an exit area of 42 mm^2 . The injector was pre-calibrated using an Alicat M-250SLPM-D/5 M mass flow meter with an uncertainty of $\pm 0.25 \text{ SLPM}$, and the discharge coefficient was measured to be 0.81. The intake and nozzle block portions of the model were manufactured as a single piece using a Stratasys Objet30 Pro 3D printer to enable the complex internal geometry of the injector to be produced at low manufacturing cost. This was mounted into an aluminum body to form the scramjet geometry.

2.3 Instrumentation

Measurements were taken of surface pressure along the body, injection pressure and temperature, and loads and moments on the model. Flowfield visualization was obtained using high-speed video schlieren. All sensor data were recorded using an NI PXIe-8135 controller with NI

PXIe-6368 acquisition cards at 200 kS/s/channel and 16 bit ADC output.

Pressure was measured along the centerline of the model and laterally upstream of the injector using tapped Honeywell SDX15A2 absolute pressure transducers with ranges of 0 to 15 psi and uncertainties of $\pm 0.2\% \text{ FS}$. Centerline gauges were placed with 20 mm spacing, and the lateral gauges were placed 20 mm upstream of the injector. Furthermore, one centerline gauge was replaced with a surface mounted Kulite XCS-093 absolute pressure transducer, with a range of 0 to 5 psi and an uncertainty of $\pm 0.1\% \text{ FS}$, to allow for a more precise calibration of the pressure sensitive paint (PSP). Another two Honeywell transducers were placed along the centerline of the bottom of the model to determine the off-set in lift due to the compressed flow between the model and the shielding. All transducers were calibrated in situ from 1 bar to vacuum during the pre-test pump down of the tunnel. A pre-calibrated Inficon CDG025D high-precision vacuum

gauge with an uncertainty of $\pm 0.2\%$ of the measured value was used as a reference gauge.

ISSI FP Porous, Fast Response Pressure Sensitive Paint (PSP) was applied to the wetted surface of the model expansion nozzle. The PSP was illuminated from above with a Luminus CBT-120 UV LED at 24 V, with a diffuser and a UV filter placed in front of it. The surface was imaged via a mirror onto a Photron FASTCAM Mini UX200 at a frame rate of 10 kfps and used a 550 nm long pass filter in front of the lens to block the UV light. The behavior of PSP can be described by the Stern–Volmer equation:

$$\frac{I_{\text{ref}}}{I} = a \cdot \left(\frac{p_{O_2}}{p_{O_2,\text{ref}}} \right)^n + b \quad (1)$$

where I is the measured light intensity and p_{O_2} is the partial pressure of oxygen at the surface. The subscript *ref* refers to a reference condition, where an intensity is measured at a known pressure. This reference state is measured for each shot before the flow initiates, while the test section is at a vacuum (50–100 Pa). The constants a , b , and n are calculated from calibration data. PSP calibration was performed in situ on a shot-by-shot basis, by taking measurements of pressure and emitted intensity at different test section pressures, using the surface mounted Kulite pressure transducer as a reference gauge. This has the advantage of accounting for the sensitivity of the paint to variations in temperature. By using the reference gauge method, the uncertainty of PSP measurements is tied to the uncertainty of the pressure sensor used (the Kulite XCS-093 gauge with an uncertainty of $\pm 0.1\%$ FS).

A 0.25 mm butt welded K-type thermocouple and an additional Honeywell SDX15A2 pressure transducer were mounted into the injector plenum. Using the assumption that the flow was stagnated in the plenum and the pre-calibrated discharge coefficient, the mass flow rate through the injector could be calculated using the choked mass flow equation. This calculation was not used in the final presentation of results; injection to stagnation pressure ratio was used instead.

A Tectis F9866 6-axis load cell with a full range of 200 N and 6 Nm and an uncertainty of $\pm 0.5\%$ FS was used to measure the forces on the model. The moment arm resulting from the arrangement of the model sting was 145 mm downstream and 61 mm below the leading edge of the model. Static calibration of all six axes to their full range was carried out prior to testing by hanging known masses from the load cell at different orientations. This allowed each axis to be calibrated in isolation. Using this method, the 95% confidence in the calibrated gradient was $< 1\%$ for each axis. The response time of the system was found to be fast enough, and the output signal was steady enough across the test time that a dynamic calibration was deemed unnecessary.

A 300-mm-diameter high-speed Z-type schlieren system, incorporating a Luminus CBT-120 green LED, was setup for the experiments. A Photron FASTCAM Mini AX100 video camera was placed at the side of the test section to image the flowfield laterally at 1280×1000 pixels, and a frame rate of 10 kfps. In addition to providing information about the flowfield, this was also used to determine the location of the injection-induced separation.

3 Results

3.1 Flowfield and injection-induced separation

The slot injection causes an effective protuberance in the surface topology that the flow has to be diverted around, causing a pressure rise. This adverse pressure gradient causes the boundary layer to separate. The FTV force may be considered to mainly result from a local increase in surface pressure in the separated boundary layer upstream of the injector. Figure 2 shows a schematic of the expected flow pattern around the model, and a frame from the schlieren imaging.

Figure 3 compares the separation distance determined from the PSP at the centerline of the exhaust surface and schlieren imaging as a function of injection pressure ratio and freestream Reynolds number. The size of the separation can be measured directly from the schlieren imaging by tracing the separation shock back to the model surface or from the processed PSP data by measuring where the pressure first deviates from the no injection baseline. In both cases, this was carried out manually by the same person to avoid any differences in the chosen location. The associated uncertainty with each method is expected to be no more than ± 2 mm. No significant unsteadiness was observed in either the PSP or schlieren. The separation distance is seen to rise

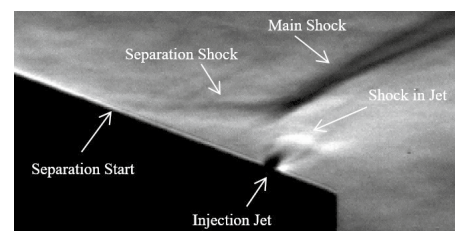
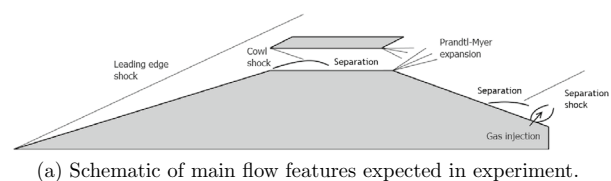


Fig. 2 Flowfield around the injector with a hypersonic crossflow

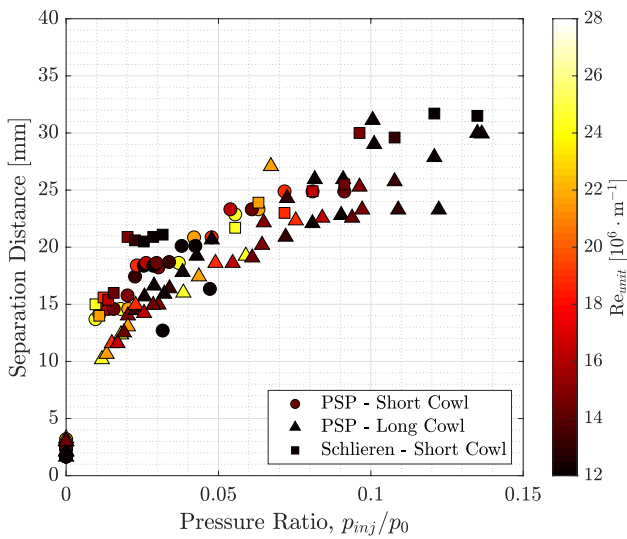


Fig. 3 Separation distances upstream of the injection location

rapidly when small amount of injection are provided, tailing-off at higher injection pressures. As expected based on investigation 2D flat plates (Kumar et al. 1997), the separation distance is largely independent of freestream Reynolds number. Results for both internal and external nozzles are comparable; however, there is suggestion that the internal exhaust tends to produce a marginally shorter separation distance.

The schlieren images evidence a lengthening of the separation distance as well as an increase in main-shock angle as the injection pressure is raised (Fig. 4). This general pattern is the same for both internal and the external nozzles. Although separation distances are approximately the same, the main-shock angle for the long cowl (internal nozzle) case is seen to be smaller. This is due to the higher pressure on the expansion surface. A reflected shock is seen to result from the boundary-layer separation in the ‘combustor’ and may also have an impact here. This is due to the shock impingement from the cowl after on the body side wall.

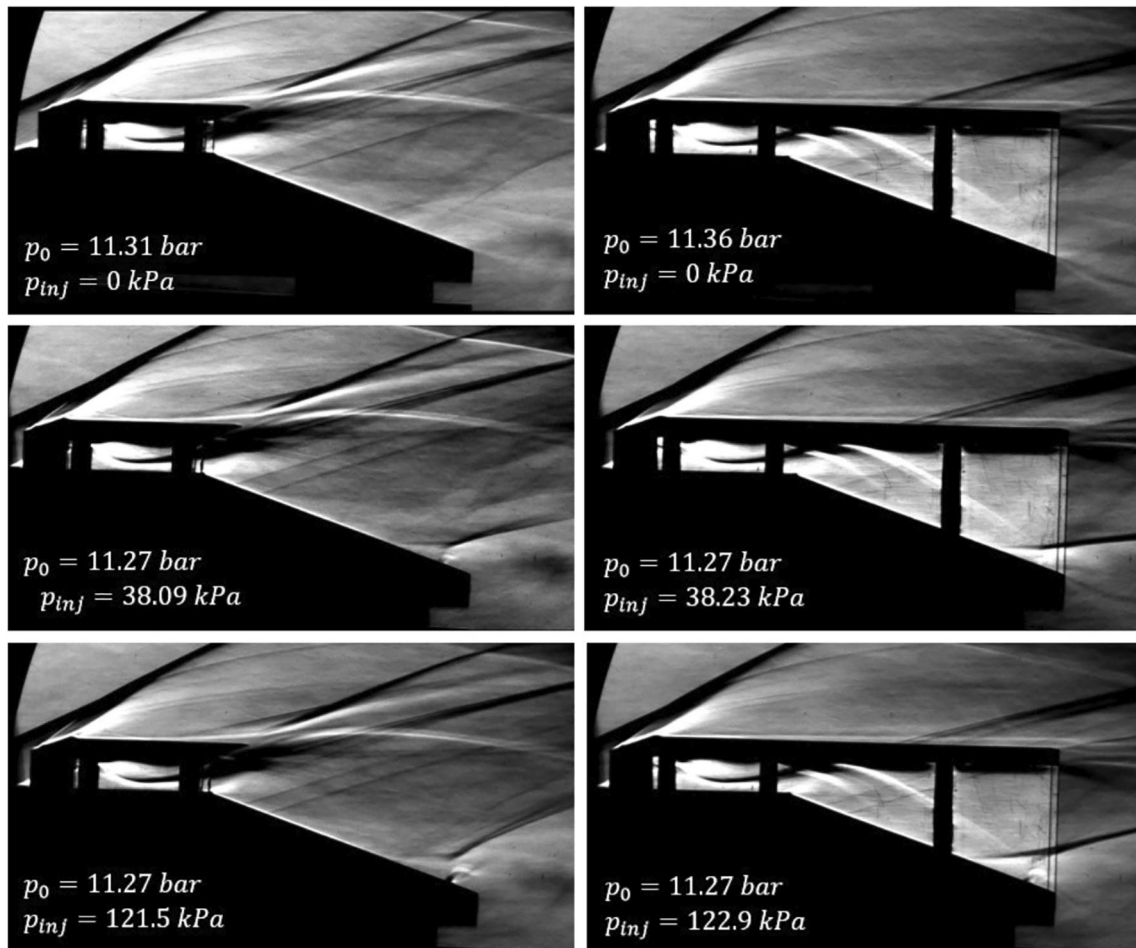


Fig. 4 Schlieren footage for several injection pressures. Left column is short cowl, and right column is long cowl

3.2 Surface pressure

Exhaust surface pressure maps comparing injection and no-injection conditions, for both internal and external nozzles, are shown in Fig. 5. These images were created by applying the Stern–Volmer equation (Eq. 1) to each pixel to convert the emitted light intensity to a surface pressure, averaged over the steady period for each test. The PSP data presented here are more useful as a tool to reveal flow features and general patterns in surface pressure rather than the exact quantification of pressures at specific locations. The lines crossing the two long cowl images are the edges of sections of the perspex cowl through which the PSP was recorded at an angle.

Both cowl configurations show an elevated pressure ahead of the injector and a reduction in pressure behind the injector when the FTV jet is present. In the short cowl (external nozzle) case, the evidence of three-dimensional spillage is clear as the pressure drops-off toward the sides of the surface. Consequently, the separated region shows high non-uniformity across the injector span in the short cowl case compared to the well-defined and consistent high pressure region in the long cowl configuration. In the center

of the long cowl images, there is evidence of the reflected shock seen in the schlieren impinging on the surface, creating a high pressure patch.

Figure 6 shows centerline pressure profiles due to FTV injection normalized to the corresponding no-injection pressure profiles. As injection pressure increases, larger peak pressure is measured upstream of the injector and the separation length increases. These data show that although separation distances are comparable between the long and short cowl configurations, the long cowl cases exhibit a marginally lower peak pressure, but a wider profile, consisting of a double rise. This double rise has been noted in previous studies (Spaid 1975), where the initial separation reaches a plateau before rising again due to the shock at the jet.

3.3 Force measurement

During the steady flow period in each test, the load cell output was found to be stable and followed the overall trend of the freestream stagnation pressure closely. Figure 7 shows a sample of filtered drag data compared to the stagnation pressure from the same test.

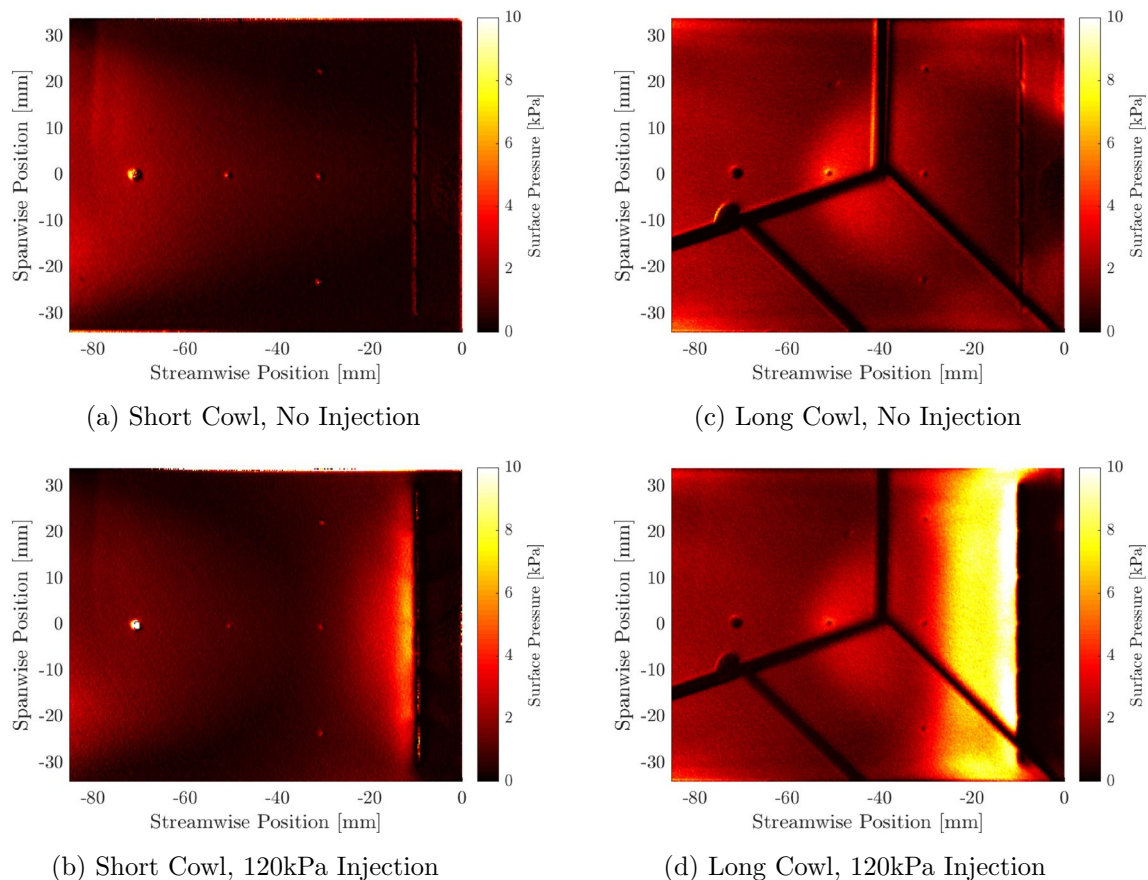


Fig. 5 Surface pressure on the expansion surface for $Re_{unit} = 13.0 \times 10^6 \text{ m}^{-1}$

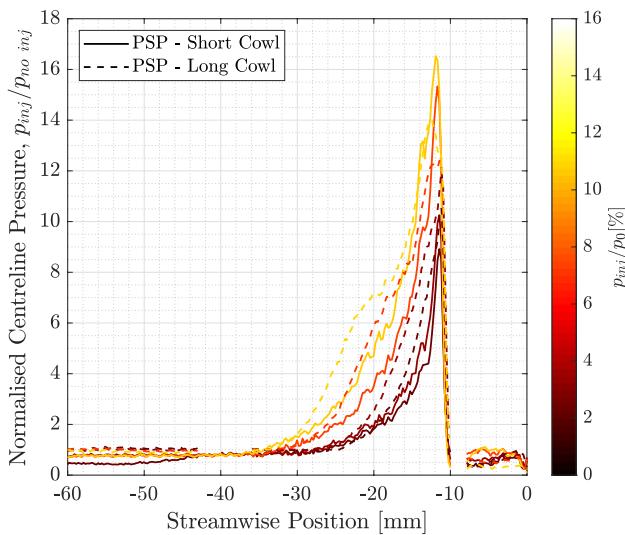


Fig. 6 Normalized centerline pressure on the expansion surface for $Re_{unit} = 13.2 \times 10^6 \text{ m}^{-1}$. The injector is located at a streamwise position of -10 mm

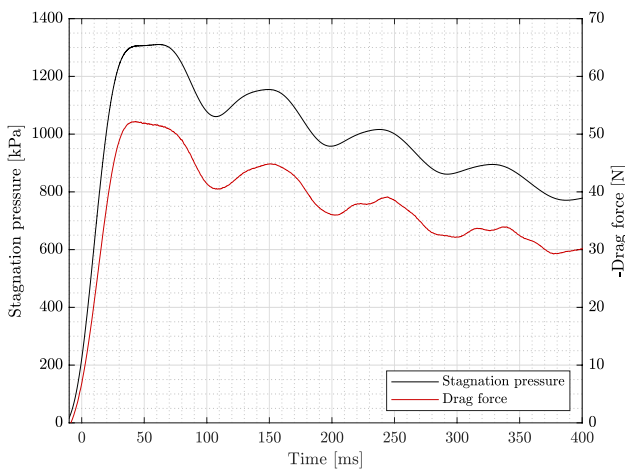


Fig. 7 Sample stagnation pressure and drag force data

The initial impulse of the flow onset caused vibrations in the experimental model which were seen as consistent small scale oscillations in the load cell output at around 100 Hz. These artifacts were removed from the load cell data by filtering before further processing. A 2-pole low-pass Chebyshev type 2 filter with a cutoff frequency of 60 Hz and a stopband attenuation of 20 dB was used on the load cell data. The highest frequency of interest was approximately 30 Hz which corresponds to the steady flow periods of 30–40 ms in length. The mean and standard deviation of the filtered signals during the steady flow periods were then used in subsequent calculations.

Lift force (L), drag force (D) and pitch moment (P) ratios are defined in Eqs. 2, 3 and 4, respectively. These ratios are

the deltas in force and moment between a shot with injection (subscript inj) and without injection (subscript $no inj$), divided by a reference force or moment. Additionally, the forces for the injection cases were scaled by the measured free stream stagnation pressure (p_0) to account for slight differences in the tunnel conditions shot-to-shot. The ratios are in the form of more conventionally used drag, lift, and pitch moment coefficient, where p_{dyn} is the freestream dynamic pressure, A_{model} is the projected capture area of the scramjet model, and l is the distance from the center of mass of the model to the position of the load cell pitch axis.

$$\text{Lift Ratio} = \frac{(L_{inj} \cdot \frac{p_0 no inj}{p_0 inj} - L_{no inj})}{p_{dyn} \cdot A_{model}} \quad (2)$$

$$\text{Drag Ratio} = \frac{(D_{inj} \cdot \frac{p_0 no inj}{p_0 inj} - D_{no inj})}{p_{dyn} \cdot A_{model}} \quad (3)$$

$$\text{Pitch Ratio} = \frac{(P_{inj} \cdot \frac{p_0 no inj}{p_0 inj} - P_{no inj})}{p_{dyn} \cdot A_{model} \cdot l} \quad (4)$$

To compare the range of conditions, the force and moment ratios are plotted against the ratio of injection pressure to freestream stagnation pressure in Figs. 8, 9 and 10. The obtained data show a strong linear relationship between the plotted ratio and the injection pressure ratio in each case and for both configurations. PSP data shown in Fig. 5 were also used to calculate lift and drag ratios, plotted in Figs. 8 and 9 as Short Cowl—PSP. These points were calculated by integrating the pressure over the expansion surface, providing a force normal to the surface. This method neglects the difference in skin friction and other surfaces being affected

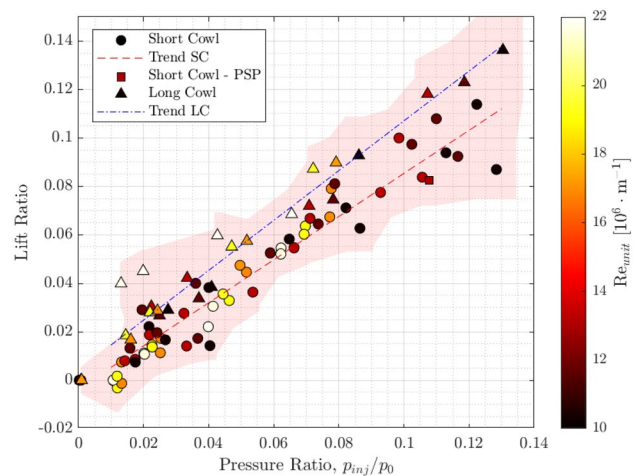


Fig. 8 Lift ratio versus pressure ratio

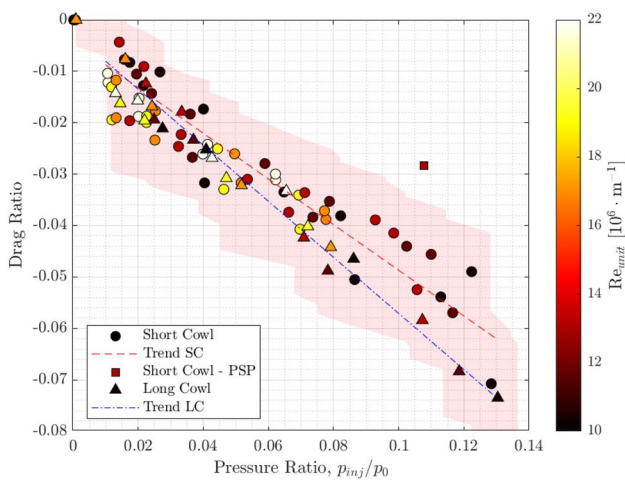


Fig. 9 Drag ratio versus pressure ratio

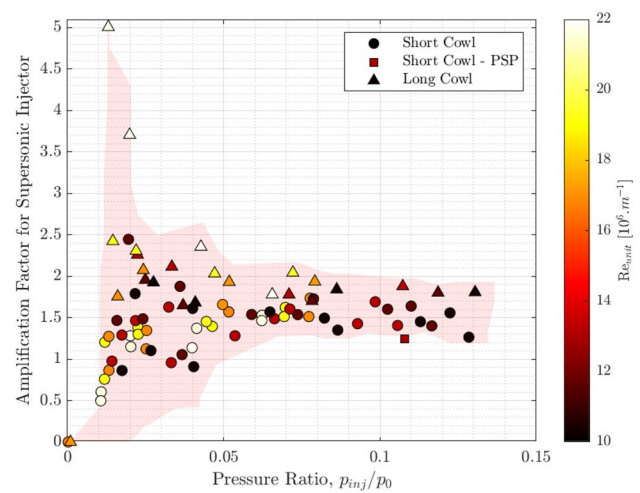


Fig. 11 Amplification factor versus pressure ratio

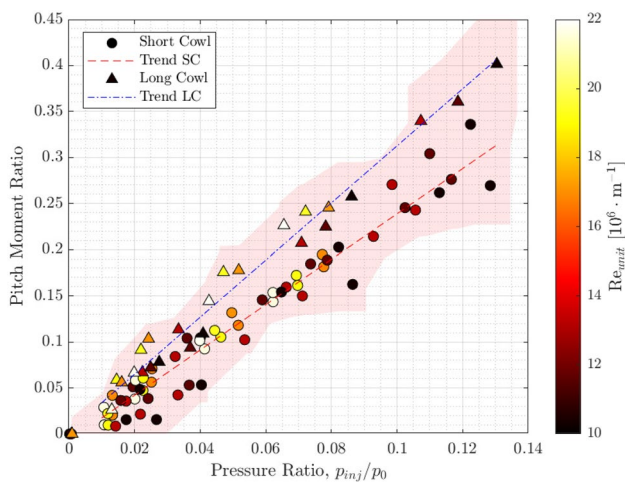


Fig. 10 Pitch ratio versus pressure ratio

by the injection, in particular the flat trailing edge of the model. Since this surface is vertical, any difference in pressure will only result in a force in the streamwise direction, hence the discrepancy in drag but not lift. Generally, Reynolds number independence is observed in the data. This agrees well with the conclusions drawn by Spaid (1975).

Although the short cowl and long cowl data are close to one-another, the internal nozzle tends to produce a slightly enhanced effect over the external nozzle configuration: the long cowl trends are marginally steeper, indicating a potential benefit in controllability of the FTV effect on a real vehicle. This may be a result of the higher average pressure on the expansion surface with the long cowl or the impinging shock noted in Fig. 4. This shock may also be the cause of boundary-layer separation even in a no-injection scenario, leading to the apparent ‘zero-offset’ in the long cowl trendlines.

The associated uncertainties for these derived quantities are plotted as red regions which encompass the uncertainties of each data point in both x and y axis data. Uncertainties in drag ratio appear larger than they are in lift and pitch moment ratios due to the smaller difference in drag force experienced. In all three cases, the uncertainties do not significantly detract from the obvious trend in the data. The method used to calculate the uncertainties for these quantities is briefly summarized in Appendix A.

3.4 Amplification factor

The interaction between a jet and a supersonic freestream is well understood and usually described by an amplification factor K (Spaid 1975). In order to develop understanding of interaction between a supersonic jet and hypersonic crossflow, an amplification factor similar to the K factor has been defined for this study (Eq. 5). The formulation used by Spaid (1975) normalizes the control force effect by a hypothetical vacuum thrust, revealing the *additional* benefit due to the fluid interactions above the baseline jetting effect. In this case, the actual thrust into vacuum (T_{vac}) was measured for the external nozzle configuration before the crossflow reached the model. The force used here (F) is the force normal to the nozzle expansion surface, rather than lift or drag which were used above. This was calculated by taking the component of the resultant force vector normal to the expansion surface. This is for comparison with Spaid’s flat plate data, where the measured force is normal to the surface.

$$\text{Amp. Factor, } K = \left(F_{inj} \cdot \frac{P_{0 \text{ no inj}}}{P_{0 \text{ inj}}} - F_{no \text{ inj}} \right) \cdot T_{vac}^{-1} \quad (5)$$

Figure 11 shows the amplification factor for each shot plotted against the injection pressure normalized by the freestream stagnation pressure. As in Figs. 8 and 9, a point derived from PSP data has also been plotted. This point shows close agreement between the two measurement techniques.

Uncertainties in amplification factor have been plotted as a red area, as with the lift, drag, and pitch ratios. At conditions with a small difference in force, the associated uncertainty in amplification factor is large. This helps to explain the large spread at low injection pressure ratios. Uncertainties at higher injection pressure ratios are relatively small, giving confidence to the effect of FTV.

Comparing the amplification factor with the K factor for a sonic injector for a flat plate (Spaid 1975), it is found to be roughly half the magnitude (typically the amplification factor is between 2 and 3). Yet, with the amplification factor ranging between 1 and 2, an increase in control force compared to a vacuum thruster of 100–200% is measured. The amplification factor for the long cowl is found to be slightly higher on average. The amplification factor for the long cowl is consistently at a slightly higher level than for the short cowl, particularly at higher injection pressures. This supports the findings from the lift, drag, and pitching moment ratios that indicate an increased FTV effectiveness when using a long cowl.

4 Conclusion

An experimental method integrating PSP, schlieren and a 6-axis load cell for investigating fluidic thrust vectoring on hypersonic aircraft has been successfully demonstrated in the Oxford High Density Tunnel. Results obtained have been comparable to previous numerical and experimental research for a similar geometry and in more abstract studies. For a fundamental scramjet model, the forces produced by an FTV system have been found to be of a similar magnitude to no-injection body forces. The ratios of the force components have clear, proportionate relations to the injection pressure ratio, and an amplification factor was found to be between 1 and 2, independent of Reynolds number and injection pressure ratio. An internal expansion nozzle configuration indicated marginal advantage over the external model tested. The long cowl also produced a more uniform pressure profile on the exhaust ramp, with a spanwise-consistent separation zone ahead of the injectors. The centerline separation distance is very similar for long and short cowl configurations, though the long cowl induced a thicker but marginally lower normalized pressure profile. The impact of a reflected shock initiated by boundary layer separation at the ‘combustor’ exit is of note and may provide opportunity for a mechanism to further enhance the FTV effect.

A Uncertainty analysis

The known uncertainties in directly measured quantities are used to calculate uncertainties in subsequently derived results. The method used to propagate uncertainties from their sources to derived quantities (described by Coleman and Steele (2018)) involves summing the squares of contributions from each variable.

$$u_r^2 = \sum_{i=1}^J \left(\frac{\partial r}{\partial X_i} \right)^2 u_{X_i}^2 \quad (6)$$

Where u_r is the overall uncertainty of the variable r which is a function of multiple measured variables: $r = f(X_i, X_{i+1}, \dots, X_J)$. The total uncertainties attributed to each measured quantity, X , are denoted by u_X , and the partial derivative term quantifies the influence of each variable, X , on the derived quantity.

The main results of this paper, Figs. 8, 9, 10 and 11, are each derived from four measured variables: total temperature, total pressure, pitot pressure, and model forces.

Uncertainties associated with the tunnel pressure sensors (stagnation pressure and pitot pressure) come entirely from sensor uncertainties due to the stability of the measurements during test times. The total temperature measurement requires more complex processing (described by Hermann et al. (2019)), and, typically, a conservative 15 K uncertainty is given to total temperature measurements in HDT.

Uncertainties in model forces are the largest of the measured quantities due to the nature of the response of the load cell. For these measurements, the uncertainty is a combination of the sensor error, the calibration uncertainties, and the standard deviation of the filtered load cell output during the steady test periods.

Acknowledgements Firstly, we would like to acknowledge the support of the USAF in funding this research under EOARD Grant FA9550-17-1-0401. Thanks to Hilbert van Pelt for recommendations and access to his original test geometry and Russ Cummings for critical review and support. Experimentation in the University of Oxford’s hypersonic facilities is only possible due to the hard work and technical expertise of our skilled team of support staff, whom the authors acknowledge gratefully.

Open Access This article is licensed under a Creative Commons Attribution 4.0 International License, which permits use, sharing, adaptation, distribution and reproduction in any medium or format, as long as you give appropriate credit to the original author(s) and the source, provide a link to the Creative Commons licence, and indicate if changes were made. The images or other third party material in this article are included in the article’s Creative Commons licence, unless indicated otherwise in a credit line to the material. If material is not included in the article’s Creative Commons licence and your intended use is not permitted by statutory regulation or exceeds the permitted use, you will need to obtain permission directly from the copyright holder. To view a copy of this licence, visit <http://creativecommons.org/licenses/by/4.0/>.

References

- Coleman HW, Steele WG (2018) *Experimentation, validation, and uncertainty analysis for engineers*. Wiley, New York
- Hermann T, McGilvray M, Hambidge C, Doherty L, Buttsworth D (2019) Total temperature measurements in the oxford high density tunnel. In: *International conference on flight vehicles, aerothermodynamics and re-entry missions and engineering*, FAR, Monopoli, Italy
- Iverson W, Hambidge C, McGilvray M, Steuer D, Hermann T, Neely AJ (2019) Fundamental experiments of fluidic thrust vectoring for a hypersonic vehicle. In: *AIAA Scitech forum*. <https://doi.org/10.2514/6.2019-1680>
- Keyes F, Frederick G (1952) The conductivity, viscosity, specific heat, and Prandtl numbers for thirteen gases. Technical report, Prog. Squid, M.I.T
- Kumar D, Stollery JL, Smith AJ (1997) Hypersonic jet control effectiveness. *Shock Waves*. <https://doi.org/10.1007/s00193005005>
- McClinton C (2006) X-43—scramjet power breaks the hypersonic barrier: Dryden lectureship in research for 2006. 44th AIAA aerospace sciences meeting and exhibit. <https://doi.org/10.2514/6.2006-1>
- McGilvray M, Doherty LJ, Neely AJ, Pearce R, Ireland P (2015) The oxford high density tunnel. In: *20th AIAA international space planes and hypersonic systems and technologies conference*, p 3548
- Skujins T, Cesnik CES, Oppenheimer MW, Doman DB (2010) Canard-elevon interactions on a hypersonic vehicle. *J Spacecr Rocket* 47(1):90–100. <https://doi.org/10.2514/1.44743>
- Spaid FW (1975) Two-dimensional jet interaction studies at large values of Reynolds and Mach numbers. *AIAA J* 13(11):1430–1434. <https://doi.org/10.2514/3.7011>
- Van Pelt H, Neely AJ, Young J, De Baar JHS (2017) A numerical study into hypersonic fluidic thrust vectoring. In: *International symposium for air breathing engines*
- Van Wie DM, Drewry DG, King DE, Hudson CM (2004) The hypersonic environment: required operating conditions and design challenges. *J Mater Sci* 39(19):5915–5924. <https://doi.org/10.1023/B:JMSE.0000041688.68135.8b>
- Wu JM (1961) Approximate analysis of thrust vector control by fluid injection. *ARS J* 31(12):1677–1685. <https://doi.org/10.2514/8.5891>

Publisher's Note Springer Nature remains neutral with regard to jurisdictional claims in published maps and institutional affiliations.